




Aluminum nitride waveguide beam splitters for integrated quantum photonic circuits

HYEONG-SOON JANG,^{1,2}  DONGHWA LEE,^{1,3} HYUNGJUN HEO,¹ YONG-SU KIM,^{1,3}  HYANG-TAG LIM,^{1,3} SEUNG-WOO JEON,¹ SUNG MOON,^{1,3} SANGIN KIM,²  SANG-WOOK HAN,^{1,3}  AND HOJOONG JUNG^{1,2,*}

¹Center for Quantum Information, Korea Institute of Science and Technology (KIST), Seoul 02792, Republic of Korea

²Department of Electrical and Computer Engineering, Ajou University, Suwon 16499, Republic of Korea

³Division of Nano and Information Technology, KIST School, Korea University of Science and Technology, Seoul 02792, Republic of Korea

*Corresponding author: hojoong.jung@kist.re.kr

Received 26 April 2022; revised 7 April 2023; accepted 5 May 2023; posted 9 May 2023 (Doc. ID 461723); published 19 June 2023

We demonstrate integrated photonic circuits for quantum devices using sputtered polycrystalline aluminum nitride (AlN) on insulator. On-chip AlN waveguide directional couplers, which are one of the most important components in quantum photonics, are fabricated and show the output power splitting ratios from 50:50 to 99:1. Polarization beam splitters with an extinction ratio of more than 10 dB are also realized from the AlN directional couplers. Using the fabricated AlN waveguide beam splitters, we observe Hong–Ou–Mandel interference with a visibility of $91.7\% \pm 5.66\%$. © 2023 Chinese Laser Press

<https://doi.org/10.1364/PRJ.461723>

1. INTRODUCTION

Recently, quantum supremacy has been demonstrated and has triggered a lot of interest in the quantum information community [1–3]. Among many candidates for quantum processors, photonic qubit-based integrated quantum circuits are emerging as a promising platform for quantum information processing by replacing the bulk quantum optics system, and they already have shown their potential for quantum computers and quantum simulators [4–7].

Traditionally, silicon has been widely used for integrated photonic circuits thanks to the mature nano-fabrication technology. For quantum device applications, however, low optical loss in a broad wavelength range and fast modulation speed are highly preferred where silicon has limited properties [8–10]. Other materials such as silica [11], silicon nitride (SiN) [12], diamond [13], and tantalum pentoxide (Ta₂O₅) [14] have limited modulation speed due to the lack of electro-optic (EO) effect. The material properties of lithium niobate (LiNbO₃) fit very well for quantum applications, but wafer bonding and smart cut technique are necessary to prepare the thin film on insulator, which needs to be developed more for cost-effective mass production [15,16]. Meanwhile, the group III–V materials including GaN, AlGaAs, InP, and aluminum nitride (AlN) provide the Pockels effect and low enough optical losses [17–19]. Especially, AlN shows the lowest optical loss among the group III–V materials and a broadband transparent window from ultraviolet (200 nm) to mid-infrared (13.6 μm) [20–22]. By taking advantages of the above properties, spontaneous parametric downconversion (SPDC) in AlN has been reported,

which cannot be performed on Si or SiN platforms [23]. In addition, AlN can be directly deposited on the insulator on Si by RF sputtering, which enables mass production due to its relatively simple and inexpensive manufacturing [24].

In this paper, we report a full set of AlN directional couplers that cover all beam splitting ratios, which is a key component for quantum photonic devices. Several AlN directional couplers have been already demonstrated [25–27]. Here, however, we fabricate more than 50 AlN directional couplers with different coupling gaps and coupling waveguide lengths, and we show their performance with high yield, which can be a good reference. In addition, we fabricate polarization beam splitters (PBSs) by adjusting the coupling conditions of TE and TM modes in the directional couplers. Furthermore, a two-photon interference experiment is performed using the 50:50 directional coupler, and the Hong–Ou–Mandel (HOM) interference with $91.7\% \pm 5.66\%$ visibility is observed without accidental coincidence counts subtraction. Detailed fabrication methods and measurement process are explained in the following.

2. SINGLE MODE WAVEGUIDE

The 500-nm-thick polycrystalline AlN thin film is deposited on 3 μm thermally grown SiO₂ on 4 inch (100 mm) Si substrate by RF sputtering. Figure 1(a) shows the measured refractive indices of the sputtered AlN thin film from 250 nm to 1650 nm wavelength range using the ellipsometry. The dashed lines are the indices of the as-deposited AlN, and the solid lines are the indices of AlN after annealing process at 950°C in N₂

environment for 1 h. After the annealing, both ordinary (n_o) and extraordinary (n_e) refractive indices are decreased over the whole measured wavelength range. The imaginary part of the refractive index or extinction coefficient (k) of AlN at the telecom band, which has to be small enough to be used for the quantum integrated circuit, is less than the reliable equipment measurement limit (1×10^{-6}) even before annealing. The high extinction coefficient at ultraviolet regime (up to 0.01 or 3.5×10^3 dB/cm) decreases dramatically after annealing, which indicates our annealing process reduces the optical absorption of the AlN thin film. We also qualitatively observe the decreased extinction coefficient from the visible to telecom band after annealing even though it is too small to be measured accurately.

To avoid modal dispersion, we engineer the geometry of AlN waveguides to support only the first order transverse electric (TE) and transverse magnetic (TM) guided modes. First, we find the eigenmode solutions and obtain the effective refractive indices at 1550 nm wavelength of 500-nm-thick AlN thin film using the Lumerical MODE solution tool. Figure 1(b) shows the simulation result of the effective indices of the four lowest order modes (TE₀₀, TM₀₀, TE₀₁, and TM₀₁). When the waveguide width increases, the electromagnetic field is more strongly confined inside of AlN than the surrounding SiO₂ cladding, which results in the increased effective index and multimode. The waveguide width less than 900 nm suppresses the higher-order modes while maintaining the fundamental mode effective refractive indices far away from the SiO₂ cladding index of 1.44.

The AlN photonic circuits are fabricated as the following process. The 500-nm-thick AlN on 3- μ m-thick SiO₂ on Si substrate is spin-coated with hydrogen silsesquioxane (HSQ) resist (FOX-15). Then, we expose patterns including straight/

curved waveguides and directional couplers using electron-beam lithography (JEOL JBX9300FS). Following that, the sample is developed and etched using inductively coupled plasma reactive ion etching (ICP RIE) with STS Multiplex ICP. The etching gases are Cl₂ and BCl₃ at a rate of 20 and 15 sccm (standard cubic centimeters per minute), respectively. The etching rate for AlN is about 160 nm/min and 130 nm/min for HSQ at an RF bias power of 100 W and ICP power of 800 W under 5 mTorr (1 Torr = 133.32 Pa) pressure. We etch the sample for 4 min, which is long enough to fully etch the 500-nm-thick AlN and short enough for 700-nm-thick HSQ to resist.

After the dry etching, the AlN waveguide with HSQ e-beam resist is checked with a scanning electron microscope (SEM) as shown in Fig. 1(c). The AlN is fully etched with enough HSQ on top of the waveguide. To cover the fabricated AlN waveguides, 2 μ m plasma enhanced chemical vapor deposition (PECVD) SiO₂ is deposited, which is enough to protect the optical modes from any optical loss sources on the device. Finally, in order to improve the optical properties of AlN, annealing is performed at 950°C in N₂ environment for 1 h. Figure 1(d) shows the cross section taken by SEM of the final AlN waveguide device with PECVD SiO₂ upper cladding and thermal SiO₂ under cladding. The device structures in this paper are the same as in Fig. 1(d) if not otherwise mentioned.

Normally, the fabricated optical waveguides are not perfectly rectangular but have some sidewall angles mainly due to the dry etching process. Especially for the coupling waveguides in which two waveguides are close to each other, the sidewall angle is different from the single waveguide's one owing to the etch-lag effect [28]. Considering these fabrication errors, coupling waveguide widths and gaps are carefully designed.

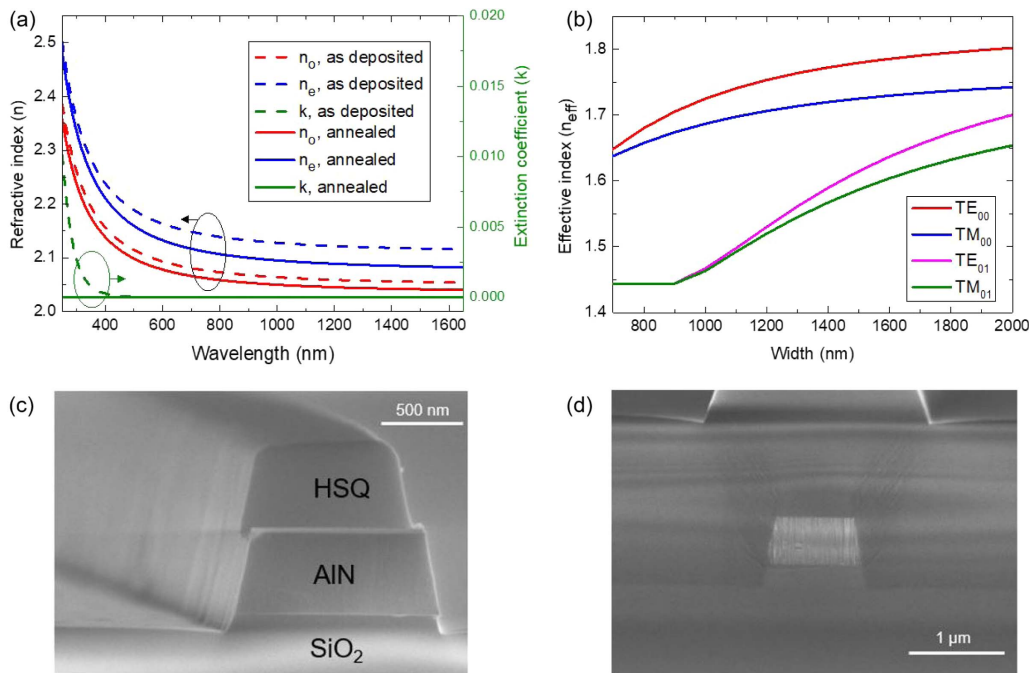


Fig. 1. (a) Measured complex refractive indices of AlN. (b) Calculated effective indices dependent on the waveguide width. Scanning electron microscope (SEM) images of the AlN waveguide (c) without top cladding and (d) with SiO₂ top cladding.

3. BEAM SPLITTER

Beam splitters are one of the key components for a photon-based information processing system including classical and quantum experiments. Optical waveguide beam splitters generally use evanescent coupling between two adjacent waveguides so that some portion of the propagating light from one optical waveguide transfers to the other optical waveguide. These beam splitters or directional couplers can also be utilized as frequency filters [29,30], mode converters [31–33], and PBSs [34–36] by additional waveguide engineering.

The directional coupler in Fig. 2(a) shows when the input power splits to 50:50 at the output ports, which depends on the coupling gap and coupling waveguide length. Figure 2(b) shows the top view of the SEM images of the fabricated AlN waveguide directional couplers. To study the output beam splitting ratio of the AlN waveguide, various directional couplers with a coupling gap from 200 nm to 700 nm and a coupling waveguide length from 1 μm to 11 μm are fabricated while the waveguide width and height are fixed to 800 nm and 500 nm, respectively.

The simulation result of the output beam splitting ratio after the directional coupler is shown in Fig. 2(c). The coupling gap and length are scanned while the through port power ratio is monitored. If the coupling gap is too large and the coupling waveguide length is too small, the evanescent wave coupling is too weak to split the input light. Therefore, the two waveguides cannot interact with each other, and 100% output

power at the through port is observed at bottom right area in the Fig. 2(c). If the coupling gap is too small and the coupling waveguide length is too long, the coupling strength becomes too strong. Thus, the coupled light couples back to its original waveguide so that the optical power between the two adjacent waveguides is periodically exchanged along with the propagation as shown in the top left area of Fig. 2(c) and in Fig. 2(e). The green area indicates a 50:50 output coupling ratio, which is the most useful for many optics experiments.

The experiment data with different coupling gaps and lengths are summarized in Fig. 2(d). All fabricated directional couplers are tested using a 1550 nm wavelength laser with TE polarization, and two lensed fibers are used for fiber-to-chip input and output coupling. We observe various output ratios from 50:50 to 1:99 with different coupling gaps and lengths, which match very well with the simulation result in Fig. 2(c). Figure 2(e) shows the simulation result of the through and coupled port power ratio at a specific coupling waveguide length of 8 μm . The coupling gap dramatically changes the output ratio. Figure 2(f) shows the measurement result of all four possible coupling cases at a coupling waveguide length of 8 μm . The simulation and experiment results match well except when the coupling gap is 200 nm, which is due to low fabrication tolerances. Based on this reference, we can realize the directional coupler with a desired splitting ratio for the beam splitter function in AlN integrated photonics.

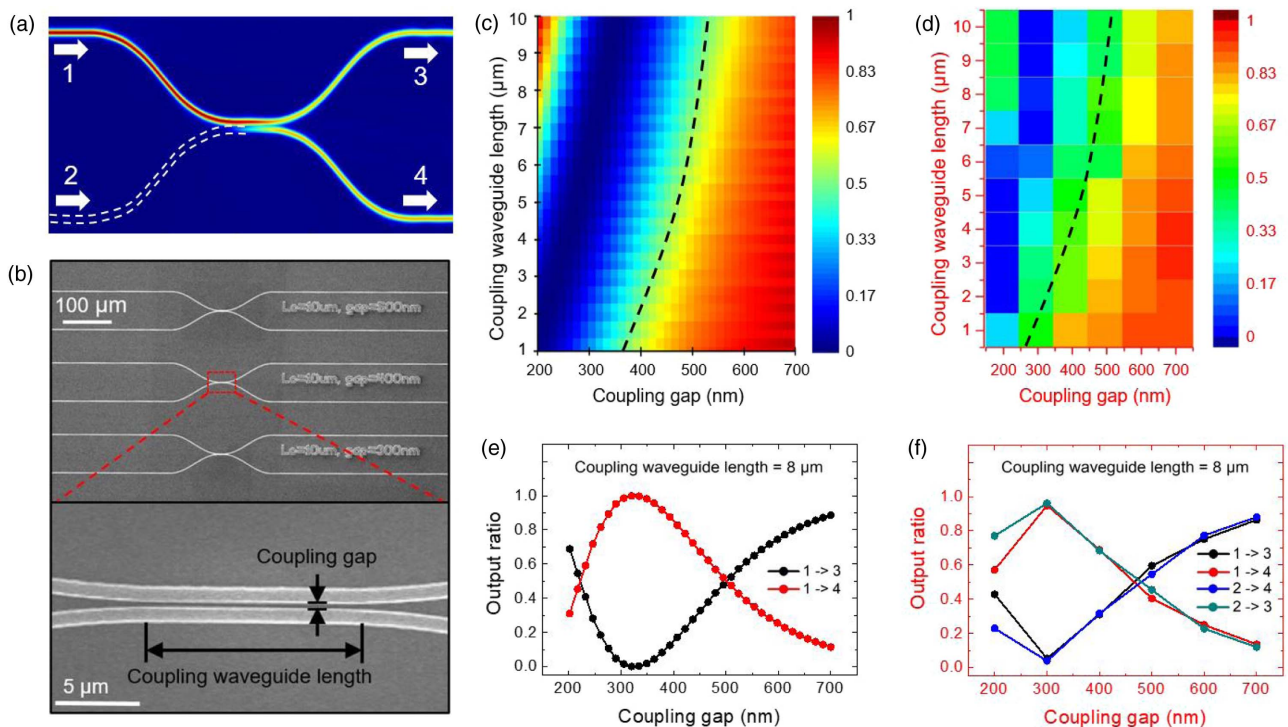


Fig. 2. Simulation, fabrication, and measurement results of directional couplers at 1550 nm wavelength and TE mode. (a) Directional coupler simulation showing 50:50 output ratio. (b) SEM image of fabricated directional couplers. (c) Simulation and (d) experiment results of the through port (1 \rightarrow 3) output ratio map obtained by changing the coupling waveguide length and gap. The black dashed lines indicate a coupling condition of 50:50 ratio. (e) Simulation and (f) experiment results of the output ratios at through (1 \rightarrow 3) and coupling (1 \rightarrow 4) ports depend on coupling gap at a fixed coupling waveguide length of 8 μm .

4. POLARIZATION BEAM SPLITTER

We used the TE mode for the above experiment, but the TM mode has a different beam splitting ratio owing to the different effective index. By utilizing this, PBSs are realized via long coupling waveguides and the different coupling strengths between TE and TM modes.

The mode in the coupling waveguides can be interpreted as the overlaps of even and odd super-modes [37]. During the two super-modes' co-propagation, the light in one waveguide is completely transferred to another waveguide when the phase difference between the even and odd super-modes is π . Therefore, the transfer distance (D_t), which is the minimum coupling wavelength length for completely transferring light to the adjacent waveguide, can be expressed using the effective index difference ($\Delta n_{\text{eff}} = n_{\text{eff}}^{\text{even}} - n_{\text{eff}}^{\text{odd}}$) between the even and odd super-modes for each polarization as below:

$$D_t^{\text{TE}} = \frac{\lambda}{2\Delta n_{\text{eff}}^{\text{TE}}}, \tag{1}$$

$$D_t^{\text{TM}} = \frac{\lambda}{2\Delta n_{\text{eff}}^{\text{TM}}}, \tag{2}$$

where λ is the light wavelength in vacuum, and D_t^{TE} and D_t^{TM} are the transfer distances of TE and TM polarizations, respectively. If the coupling waveguide length matches with the integer of the transfer distance (D_t), the light transfer to the adjacent waveguide occurs periodically. As the TE and TM modes have different effective indices, their transfer distances

are different as well. Thus, we can find the length of the coupling waveguide, which splits the TE and TM modes to different output ports. In our design, D_t^{TE} is larger than D_t^{TM} , and the transfer distance for the PBS (D_{PBS}) can be expressed as follows:

$$D_{\text{PBS}} = nD_t^{\text{TE}} = (n + m)D_t^{\text{TM}},$$

$$\text{for } n = 1, 2, 3, \dots, \quad m = 1, 3, 5, \dots \tag{3}$$

To minimize the device footprint, we fix the m to 1, which is also a practical solution. Then, we define the polarization diversity parameter ΔD_t as follows:

$$\Delta D_t = \frac{nD_t^{\text{TE}} - (n + 1)D_t^{\text{TM}}}{D_t^{\text{TM}}}, \quad \text{for } n = 1, 2, 3, \dots \tag{4}$$

The normalized unitless parameter ΔD_t needs to be 0 to satisfy the PBS. Figure 3(a) shows the simulation result of ΔD_t depending on the coupling gap for different n at 1550 nm wavelength. There are specific gaps that satisfy $\Delta D_t = 0$ for different n . For example, when $n = 4$ (magenta line, $4D_t^{\text{TE}} = 5D_t^{\text{TM}}$), the line crosses 0 when a coupling gap is near 600 nm, which means the TE mode couples back and forth 4 times to the adjacent waveguide while the TM mode couples 5 times with the same coupling waveguide length.

The smaller gaps require the larger integer n to satisfy D_{PBS} , owing to the small effective index difference of TE and TM modes. However, the small gap enhances the coupling strength so that the overall transfer distance for the PBS is shortened as shown in Fig. 3(b). Considering the fabrication tolerance and

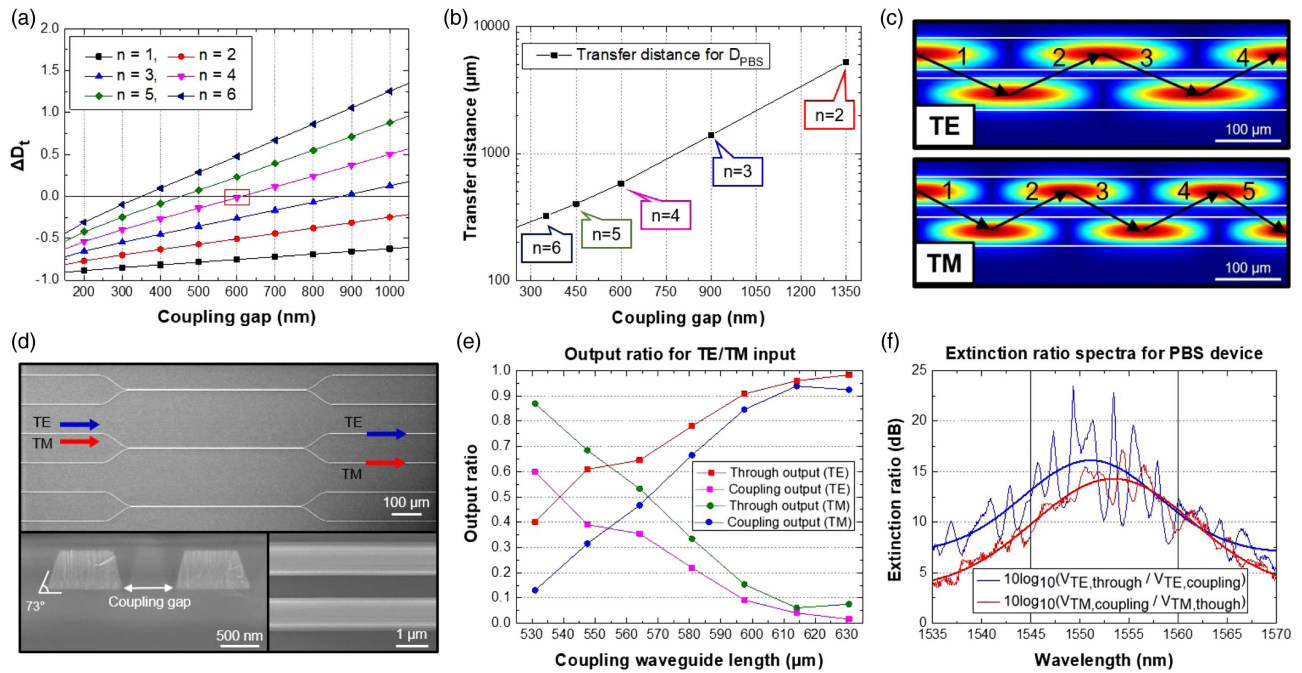


Fig. 3. (a) Calculated ΔD_t dependent on the coupling gap at 1550 nm wavelength. (b) Calculated PBS transfer distance (D_{PBS}) with different n , thus different coupling gap. (c) Coupling simulation in the case of $n = 4$ condition when TE or TM modes are launched in the upper waveguide. Waveguide width, 700 nm. (d) SEM images of fabricated directional couplers for PBS. Up, top view; bottom left, cross section of coupling part; bottom right, top view zoom in of coupling part. (e) Measured output ratio for TE/TM input with different coupling waveguide lengths at 1550 nm wavelength and 600 nm gap. (f) Measured extinction ratios and their Gaussian fitting for TE (blue) and TM (red) inputs from the PBS with a gap of 600 nm and a coupling waveguide length of 614 μm .

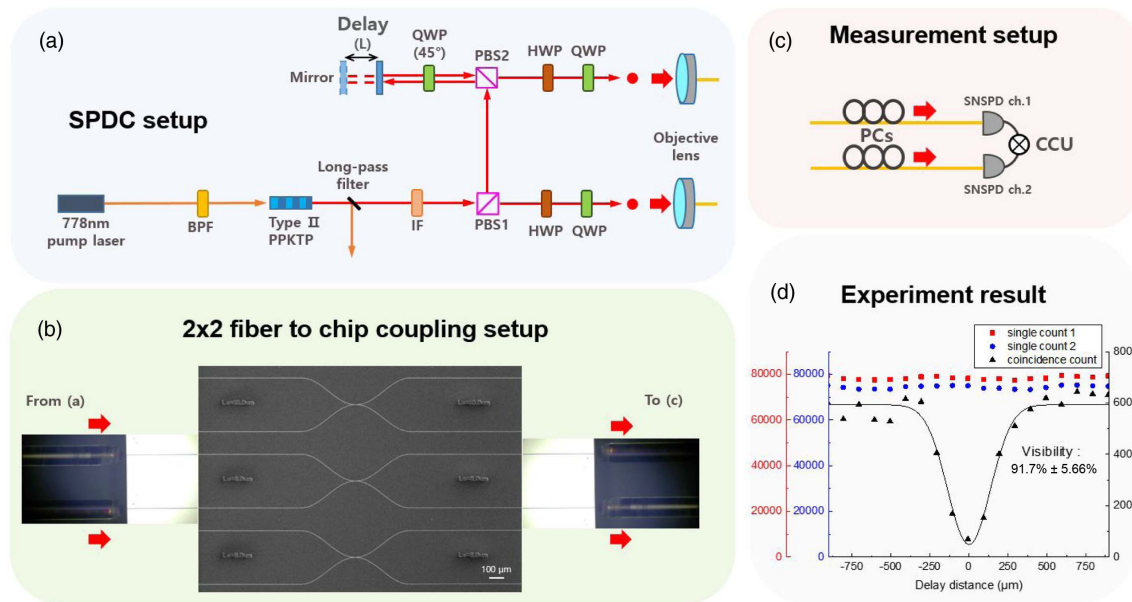


Fig. 4. (a) SPDC setup for single photon pairs generation. (b) Lensed fibers to chip coupling setup scheme of two inputs and two outputs. (c) Twofold coincidence counting measurement setup. (d) HOM interference result from the AlN waveguide beam splitter. The integration time of the photon count for the y axis is 10 s.

footprint, the $n = 4$ condition is selected, which requires a gap of ~ 600 nm and a coupling waveguide length of ~ 600 μm . Figure 3(c) shows the TE and TM mode coupling simulation from the above parameters. While the TE mode crosses the waveguide 4 times, the TM mode crosses the waveguide 5 times with the same transfer distance, which results in polarization-dependent beam splitting. From the simulated parameters, we fabricate the AlN PBS based on the directional coupler as shown in Fig. 3(d), in which the SEM images show the top view (up), cross section (bottom left), and zoom-in (bottom right) of the couplers. The fabricated waveguide width at half-height is 850 nm, and the sidewall angle is about 73° .

The measurement results are shown in Figs. 3(e) and 3(f). Figure 3(e) shows the output ratio of TE and TM modes with various coupling waveguide lengths and a fixed coupling gap of 600 nm. The red and magenta squares indicate the TE mode output power ratios at the through and coupled ports, respectively, and the green and blue circles indicate the TM mode output power ratios at the through and coupled ports, respectively. When the coupling waveguide length is 614–630 μm , the TE mode propagates to the through port while the TM mode goes to the coupled port with extinction ratio >10 dB at 1550 nm wavelength.

As the coupling is sensitive to the wavelength, we test the wavelength tolerance using the device with a gap of 600 nm and a coupling waveguide length of 614 μm , as shown in Fig. 3(f). The PBS shows high extinction ratio (>10 dB) within 1545–1560 nm wavelength range for both TE and TM modes. The fluctuations in the data are caused by Fabry–Perot interference that can be observed in wavelength-dependent chip measurements [38]. We expect a higher extinction ratio with better wavelength tolerance when the cascaded PBS is realized.

5. QUANTUM EXPERIMENT

Now, using the fabricated AlN directional coupler with an output ratio of 50:50 in TM mode and with a 3 dB bandwidth of 123.5 nm wavelength, we measure two-photon quantum interference using a single photon pair generated from an SPDC and observe the HOM interference [39].

Figure 4(a) shows the SPDC setup for identical two-photon generation at 1556 nm wavelength by 10-mm-long type-II periodically poled KTP crystal pumped by femtosecond laser pulses with 125 MHz repetition rate and a bandwidth of 7.5 nm at a center wavelength of 778 nm. The generated two orthogonally polarized photons (single and idler photons) pass through an interference filter (IF) with 3 nm bandwidth and are split by a free space PBS1. The input delay (L) for the idler photon is adjusted using a translational stage after PBS2 and a quarter-wave plate (QWP) at 45° . Additional QWPs and half-wave plates (HWPs) before the fiber channels ensure the TM polarization at the AlN directional coupler in Fig. 4(b).

Figure 4(b) shows the SEM image of AlN beam splitters and the picture of the actual 2×2 fiber-to-chip coupling setup. Four independently adjustable lensed fibers are used for fiber-to-chip coupling. By measuring the optical transmission power of the waveguides with different lengths, the estimated propagation loss is 2.12 dB/cm. Thus, the total propagation and coupling losses of the 8.5 mm chip are 1.8 dB and 3.7 dB/facet, respectively. The single photon pairs come from the left two optical fibers and go out to the right two optical fibers, which are connected to the measurement setup in Fig. 4(c).

We use superconducting nanowire single photon detectors (SNSPDs), which have about 80% single photon detection efficiency. The polarization state is optimized by polarization controllers (PCs) in front of the SNSPD. The twofold

coincidence counts are registered by a homemade coincidence counting unit (CCU) [40]. When the optical delay difference between the two paths is zero, two photons come out from the same outputs together, either upper or lower ports. By this HOM interference, there would be no coincidence counts between the two SNSPD channels. The measured HOM interference visibility from the actual counts is $91.7\% \pm 5.66\%$ without any post-processing such as accidental coincidence count subtraction [Fig. 4(d)]. The main reason for the HOM visibility degradation is due to the polarization misalignment, which deteriorates the indistinguishability of the photon pairs. However, our experimental results achieve the interference visibility beyond the classical limits (visibility $\geq 50\%$) [41,42], which shows that quantum optical experiments can be performed with AlN directional couplers.

6. CONCLUSION

In conclusion, we fabricated a set of AlN optical waveguide directional couplers, which cover a variety of splitting ratios from 50:50 to 1:99, by engineering the coupling gap and length. Utilizing the splitting ratio difference of the TE and TM modes in directional couplers, AlN waveguide PBSs were also realized by simply increasing the coupling waveguide length. Furthermore, a two-photon interference—the HOM effect—was demonstrated using the 50:50 directional coupler that proves the potential of the AlN photonics platform for quantum optical applications. This study can be a reference for the design and fabrication of AlN devices including directional couplers, which are a critical component especially for quantum photonics. The addition of fast modulation using the Pockels effect of AlN would enhance the functionality of AlN devices for quantum applications, and we expect quantum information processing devices such as quantum computing and quantum key distribution devices to be realized using the AlN platform in the near future.

Funding. Korea Institute of Science and Technology (2E32241, 2E32801); National Research Council of Science and Technology (CAP21031-200); Institute for Information and Communications Technology Promotion (2020-0-00947, 2020-0-00972); National Research Foundation of Korea (2019M3E4A1079777, 2021M1A2A2043892).

Disclosures. The authors declare no conflicts of interest.

Data Availability. Data underlying the results presented in this paper are not publicly available at this time but may be obtained from the authors upon reasonable request.

REFERENCES

1. F. Arute, K. Arya, R. Babbush, D. Bacon, J. C. Bardin, R. Barends, R. Biswas, S. Boixo, F. G. S. L. Brandao, D. A. Buell, B. Burkett, Y. Chen, Z. Chen, B. Chiaro, R. Collins, W. Courtney, A. Dunsworth, E. Farhi, B. Foxen, A. Fowler, C. Gidney, M. Giustina, R. Graff, K. Guerin, S. Habegger, M. P. Harrigan, M. J. Hartmann, A. Ho, M. Hoffmann, T. Huang, T. S. Humble, S. V. Isakov, E. Jeffrey, Z. Jiang, D. Kafri, K. Kechedzhi, J. Kelly, P. V. Klimov, S. Knysh, A. Korotkov, F. Kostritsa, D. Landhuis, M. Lindmark, E. Lucero, D. Lyakh, S. Mandrà, J. R. McClean, M. McEwen, A. Megrant, X. Mi, K. Michielsen, M. Mohseni, J. Mutus, O. Naaman, M. Neeley, C. Neill, M. Y. Niu, E. Ostby, A. Petukhov, J. C. Platt, C. Quintana, E. G. Rieffel, P. Roushan, N. C. Rubin, D. Sank, K. J. Satzinger, V. Smelyanskiy, K. J. Sung, M. D. Trevithick, A. Vainsencher, B. Villalonga, T. White, Z. J. Yao, P. Yeh, A. Zalcman, H. Neven, and J. M. Martinis, "Quantum supremacy using a programmable superconducting processor," *Nature* **574**, 505–510 (2019).
2. H.-S. Zhong, H. Wang, Y.-H. Deng, M.-C. Chen, L.-C. Peng, Y.-H. Luo, J. Qin, D. Wu, X. Ding, Y. Hu, P. Hu, X.-Y. Yang, W.-J. Zhang, H. Li, Y. Li, X. Jiang, L. Gan, G. Yang, L. You, Z. Wang, L. Li, N.-L. Liu, C.-Y. Lu, and J.-W. Pan, "Quantum computational advantage using photons," *Science* **370**, 1460–1463 (2020).
3. S. Ebadi, T. T. Wang, H. Levine, A. Keesling, G. Semeghini, A. Omran, D. Bluvstein, R. Samajdar, H. Pichler, W. W. Ho, S. Choi, S. Sachdev, M. Greiner, V. Vuletić, and M. D. Lukin, "Quantum phases of matter on a 256-atom programmable quantum simulator," *Nature* **595**, 227–232 (2021).
4. J. Wang, F. Sciarrino, A. Laing, and M. G. Thompson, "Integrated photonic quantum technologies," *Nat. Photonics* **14**, 273–284 (2020).
5. A. W. Elshaari, W. Pernice, K. Srinivasan, O. Benson, and V. Zwiller, "Hybrid integrated quantum photonic circuits," *Nat. Photonics* **14**, 285–298 (2020).
6. E. Pelucchi, G. Fagas, I. Aharonovich, D. Englund, E. Figueroa, Q. Gong, H. Hannes, J. Liu, C.-Y. Lu, N. Matsuda, J.-W. Pan, F. Schreck, F. Sciarrino, C. Silberhorn, J. Wang, and K. D. Jöns, "The potential and global outlook of integrated photonics for quantum technologies," *Nat. Rev. Phys.* **4**, 194–208 (2022).
7. D. Lee, J. Lee, S. Hong, H.-T. Lim, Y.-W. Cho, S.-W. Han, H. Shin, J. ur Rehman, and Y.-S. Kim, "Error-mitigated photonic variational quantum eigensolver using a single-photon ququart," *Optica* **9**, 88–95 (2022).
8. X. Xiao, H. Xu, X. Li, Y. Hu, K. Xiong, Z. Li, T. Chu, Y. Yu, and J. Yu, "25 Gbit/s silicon microring modulator based on misalignment-tolerant interleaved PN junctions," *Opt. Express* **20**, 2507–2515 (2012).
9. M. Nedeljkovic, R. Soref, and G. Z. Mashanovich, "Free-carrier electrorefraction and electroabsorption modulation predictions for silicon over the 1–14- μm infrared wavelength range," *IEEE Photon. J.* **3**, 1171–1180 (2011).
10. W. Bludau, A. Onton, and W. Heinke, "Temperature dependence of the band gap of silicon," *J. Appl. Phys.* **45**, 1846–1848 (1974).
11. H. Lee, T. Chen, J. Li, O. Painter, and K. J. Vahala, "Ultra-low-loss optical delay line on a silicon chip," *Nat. Commun.* **3**, 867 (2012).
12. A. Gondarenko, J. S. Levy, and M. Lipson, "High confinement micron-scale silicon nitride high Q ring resonator," *Opt. Express* **17**, 11366–11370 (2009).
13. M. J. Burek, Y. Chu, M. S. Z. Liddy, P. Patel, J. Rochman, S. Meesala, W. Hong, Q. Quan, M. D. Lukin, and M. Lončar, "High quality-factor optical nanocavities in bulk single-crystal diamond," *Nat. Commun.* **5**, 5718 (2014).
14. H. Jung, S.-P. Yu, D. R. Carlson, T. E. Drake, T. C. Briles, and S. B. Papp, "Tantala Kerr-nonlinear integrated photonics," *Optica* **8**, 811–817 (2021).
15. E. L. Wooten, K. M. Kissa, A. Yi-Yan, E. J. Murphy, D. A. Lafaw, P. F. Hallemeier, D. Maack, D. V. Attanasio, D. J. Fritz, G. J. McBrien, and D. E. Bossi, "A review of lithium niobate modulators for fiber-optic communications systems," *IEEE J. Sel. Top. Quantum Electron.* **6**, 69–82 (2000).
16. D. Zhu, L. Shao, M. Yu, R. Cheng, B. Desiatov, C. J. Xin, Y. Hu, J. Holzgrafe, S. Ghosh, A. Shams-Ansari, E. Puma, N. Sinclair, C. Reimer, M. Zhang, and M. Lončar, "Integrated photonics on thin-film lithium niobate," *Adv. Opt. Photon.* **13**, 242–352 (2021).
17. L. Chang, W. Xie, H. Shu, Q.-F. Yang, B. Shen, A. Boes, J. D. Peters, W. Jin, C. Xiang, S. Liu, G. Moille, S.-P. Yu, X. Wang, K. Srinivasan, S. B. Papp, K. Vahala, and J. E. Bowers, "Ultra-efficient frequency comb generation in AlGaAs-on-insulator microresonators," *Nat. Commun.* **11**, 1331 (2020).
18. C. Xiong, W. H. P. Pernice, and H. X. Tang, "Low-loss, silicon integrated, aluminum nitride photonic circuits and their use for electro-optic signal processing," *Nano Lett.* **12**, 3562–3568 (2012).

19. R. A. Griffin, S. K. Jones, N. Whitbread, S. C. Heck, and L. N. Langley, "InP Mach-Zehnder modulator platform for 10/40/100/200-Gb/s operation," *IEEE J. Sel. Top. Quantum Electron.* **19**, 158–166 (2013).
20. Y. Taniyasu, M. Kasu, and T. Makimoto, "An aluminium nitride light-emitting diode with a wavelength of 210 nanometres," *Nature* **441**, 325–328 (2006).
21. P. T. Lin, H. Jung, L. C. Kimerling, A. Agarwal, and H. X. Tang, "Low-loss aluminium nitride thin film for mid-infrared microphotonics," *Laser Photon. Rev.* **8**, L23–L28 (2014).
22. H. Jung, R. Stoll, X. Guo, D. Fischer, and H. X. Tang, "Green, red, and IR frequency comb line generation from single IR pump in AlN micro-ring resonator," *Optica* **1**, 396–399 (2014).
23. X. Guo, C.-L. Zou, C. Schuck, H. Jung, R. Cheng, and H. X. Tang, "Parametric down-conversion photon-pair source on a nanophotonic chip," *Light Sci. Appl.* **6**, e16249 (2017).
24. H. Jung and H. X. Tang, "Aluminum nitride as nonlinear optical material for on-chip frequency comb generation and frequency conversion," *Nanophotonics* **5**, 263–271 (2016).
25. M. Stegmaier and W. H. Pernice, "Broadband directional coupling in aluminum nitride nanophotonic circuits," *Opt. Express* **21**, 7304–7315 (2013).
26. B. Dong, X. Luo, S. Zhu, M. Li, D. Hasan, L. Zhang, S. J. Chua, J. Wei, Y. Chang, G.-Q. Lo, K. W. Ang, D.-L. Kwong, and C. Lee, "Aluminum nitride on insulator (AlNOI) platform for mid-infrared photonics," *Opt. Lett.* **44**, 73–76 (2019).
27. T.-J. Lu, M. Fanto, H. Choi, P. Thomas, J. Steidle, S. Mouradian, W. Kong, D. Zhu, H. Moon, K. Berggren, J. Kim, M. Soltani, S. Preble, and D. Englund, "Aluminum nitride integrated photonics platform for the ultraviolet to visible spectrum," *Opt. Express* **26**, 11147–11160 (2018).
28. I. W. Rangelow, "Critical tasks in high aspect ratio silicon dry etching for microelectromechanical systems," *J. Vac. Sci. Technol. A* **21**, 1550–1562 (2003).
29. T. Fujisawa, J. Takano, Y. Sawada, T. Sakamoto, T. Matsui, K. Nakajima, and K. Saitoh, "A novel Si four-wavelength multiplexer for 100/400 GbE using higher-order mode composed of (a)symmetric directional couplers and TE₁-TM₀ mode converter," *Opt. Express* **27**, 36286–36296 (2019).
30. J. Sakamoto, T. Goh, S. Katayose, K. Watanabe, M. Itoh, and T. Hashimoto, "Compact and low-loss RGB coupler using mode-conversion waveguides," *Opt. Commun.* **420**, 46–51 (2018).
31. Y. Ding, L. Liu, C. Peucheret, and H. Ou, "Fabrication tolerant polarization splitter and rotator based on a tapered directional coupler," *Opt. Express* **20**, 20021–20027 (2012).
32. L. Liu, Y. Ding, K. Yvind, and J. M. Hvam, "Silicon-on-insulator polarization splitting and rotating device for polarization diversity circuits," *Opt. Express* **19**, 12646–12651 (2011).
33. J. Wang, B. Niu, Z. Sheng, A. Wu, X. Wang, S. Zou, M. Qi, and F. Gan, "Design of a SiO₂ top-cladding and compact polarization splitter-rotator based on a rib directional coupler," *Opt. Express* **22**, 4137–4143 (2014).
34. H. Fukuda, K. Yamada, T. Tsuchizawa, T. Watanabe, H. Shinjima, and S. Itabashi, "Ultrasmall polarization splitter based on silicon wire waveguides," *Opt. Express* **14**, 12401–12408 (2006).
35. T. Uematsu, T. Kitayama, Y. Ishizaka, and K. Saitoh, "Ultra-broadband silicon-wire polarization beam combiner/splitter based on a wavelength insensitive coupler with a point-symmetrical configuration," *IEEE Photon. J.* **6**, 4500108 (2014).
36. Z. Lu, Y. Wang, F. Zhang, N. A. F. Jaeger, and L. Chrostowski, "Wideband silicon photonic polarization beamsplitter based on point-symmetric cascaded broadband couplers," *Opt. Express* **23**, 29413–29422 (2015).
37. Z. Gong, R. Yin, W. Ji, J. Wang, C. Wu, X. Li, and S. Zhang, "Optimal design of DC-based polarization beam splitter in lithium niobate on insulator," *Opt. Commun.* **396**, 23–27 (2017).
38. W. H. P. Pernice, C. Xiong, and H. X. Tang, "High Q micro-ring resonators fabricated from polycrystalline aluminum nitride films for near infrared and visible photonics," *Opt. Express* **20**, 12261–12269 (2012).
39. I. Kim, D. Lee, S. Hong, Y.-W. Cho, K. J. Lee, Y.-S. Kim, and H.-T. Lim, "Implementation of a 3 × 3 directionally-unbiased linear optical multiplex," *Opt. Express* **29**, 29527–29540 (2022).
40. B. K. Park, Y. S. Kim, Y. W. Cho, S. Moon, and S. W. Han, "Arbitrary configurable 20-channel coincidence counting unit for multi-qubit quantum experiment," *Electronics* **10**, 569 (2021).
41. J. G. Rarity, P. R. Tapster, and R. Loudon, "Non-classical interference between independent sources," *J. Opt. B* **7**, S171–S175 (2005).
42. Y.-S. Kim, O. Slattery, P. S. Kuo, and X. Tang, "Conditions for two-photon interference with coherent pulses," *Phys. Rev. A* **87**, 063843 (2013).